metals

MDPI

Article

Porous γ-TiAl Structures Fabricated by Electron Beam Melting Process

Ashfaq Mohammad [1,*], Abdulrahman M. Alahmari [1,2], Khaja Moiduddin [2], Muneer Khan Mohammed [1], Abdulrahman Alomar [2] and Ravi Kottan Renganayagalu [3]

Received: 17 November 2015; Accepted: 13 January 2016; Published: 18 January 2016
Academic Editor: Hugo F. Lopez

1 Princess Fatima Alnijiris's Research Chair for Advanced Manufacturing Technology (FARCAMT), Advanced Manufacturing Institute, King Saud University, Riyadh 11421, Saudi Arabia; alahmari@ksu.edu.sa (A.M.A.); muneer0649@gmail.com (M.K.M.)
2 Industrial Engineering Department, College of Engineering, King Saud University, Riyadh 11421, Saudi Arabia; kmoiduddin@gmail.com (K.M.); alomar.ab@gmail.com (A.A.)
3 Structural Nanomaterials Laboratory, PSG Institute of Advanced Studies, Coimbatore 641004, India; krravi.psgias@gmail.com
* Correspondence: mashfaq@ksu.edu.sa; Tel.: +966-1146-97372; Fax: +966-1-146-78657

Abstract: Porous metal structures have many benefits over fully dense structures for use in bio-implants. The designs of porous structures can be made more sophisticated by altering their pore volume and strut orientation. Porous structures made from biocompatible materials such as titanium and its alloys can be produced using electron-beam melting, and recent reports have shown the biocompatibility of titanium aluminide (γ-TiAl). In the present work, we produced porous γ-TiAl structures by electron-beam melting, incorporating varying pore volumes. To achieve this, the individual pore dimensions were kept constant, and only the strut thickness was altered. Thus, for the highest pore volume of ~77%, the struts had to be as thin as half a millimeter. To accomplish such fine struts, we used various beam currents and scan strategies. Microscopy showed that selecting a proper scan strategy was most important in producing these fine struts. Microcomputed tomography revealed no major gaps in the struts, and the fine struts displayed compressive stiffness similar to that of natural bone. The characteristics of these highly-porous structures suggest their promise for use in bio-implants.

Keywords: additive manufacturing; electron beam melting; titanium aluminides; porous structures; bio-implants; compressive stiffness

1. Introduction

Porous structures have many advantages over solid ones. For example, implants with porous structures exhibit better bone ingrowth [1]. In addition to this, porous structures are naturally lightweight, and porous implants induce less stress shielding than do fully solid ones [2]. Porous structures are relevant in many other applications as well, including ultra-lightweight structures, thermal equipment, and electrochemical devices [3].

Over the last decade, several researchers have tried to fabricate porous structures by using electron beam melting (EBM), an additive manufacturing process. Most of these reports dealt with Ti-6Al-4V alloy, a popular bio-implant material [4–6], demonstrating that EBM could produce high-quality porous structures. For example, Li *et al.* produced pores as small as 1 mm and struts with a thickness of only 0.5 mm [7]. Other works focused on using EBM to fabricate structures from more materials, such as stainless steels, niobium alloys, and copper [8–10]. Similarly, Cormier *et al.* used EBM to fabricate γ-TiAl, giving some positive results [11]. Processing γ-TiAl by EBM was motivated by the alloy's

potential use in aeroturbine manufacturing. Until this EBM study, γ-TiAl was used little because it was difficult to machine, forge, and cast [12,13].

Rivera-Denizard *et al.* argued that γ-TiAl has certain advantages over Ti-6Al-4V as a bio-implant material [14]. For instance, γ-TiAl does not contain vanadium, a toxic element; aluminum oxide, the predominant oxide of γ-TiAl, might prove better than titanium oxide, which erodes easily. These assumptions were tested by *in vitro* experiments that showed γ-TiAl was indeed biocompatible with osteoblast cells. Santiago-Medina *et al.* in a later work suggested that γ-TiAl's biocompatibility could be further improved with suitable surface treatments [15].

Considering the potential uses of γ-TiAl in bio-implants and aircraft turbines, the ability to produce porous structures of this alloy could give designers an edge. However, there are few reports on porous γ-TiAl; in the only report of note, Hernandez *et al.* produced stochastic foams of γ-TiAl by EBM [16]. In the current work, we aim to produce γ-TiAl structures with designed porosity. We attempted to fabricate porous γ-TiAl samples with various pore volume percentages by varying the strut thickness from 1.5 mm to 0.5 mm. From these results, we analyze and discuss how the beam current, strut thickness, and scanning strategy affected the dimensional accuracy, microstructure, and mechanical behavior of EBM-fabricated porous γ-TiAl alloy.

2. Experimental Section

γ-TiAl powder with a nominal composition of Ti-48Al-2Cr-2Nb (at. %) supplied by ARCAM AB was used as feedstock material. The powder particles were 45–150 μm in size with a mean of 110 μm, as measured by laser diffraction particle sizing technique (Mastersizer 2000, Malvern Instruments, Worcestershire, UK) (Figure 1). The particle morphology was essentially spherical, with smaller satellite particles adhering to larger ones (Figure 2). EBM was performed on an ARCAM A2 machine (ARCAM AB, Mölndal, Sweden). Each layer was set to be 90 μm thick. More details on EBM can be found elsewhere [17]. Samples were built on a 10 mm thick stainless steel support plate (area of 100 × 100 mm).

First, the porous structures were designed using CAD software (CATIA, Dassault Systèmes, Vélizy-Villacoublay Cedex, France). These files were saved in STL format and then transferred to Magics (Ver.17) software (Materialise NV, Leuven, Belgium), in which the files were checked for errors, such as missing or inverted triangles. The qualified files were then transferred to Arcam's Build Assembler software (ARCAM AB, Mölndal, Sweden). This software converts the STL geometry into thin slices and writes the output as a machine-specific ABF file. This ABF file contains all the instructions needed for a machine-control program to build the final part layer by layer.

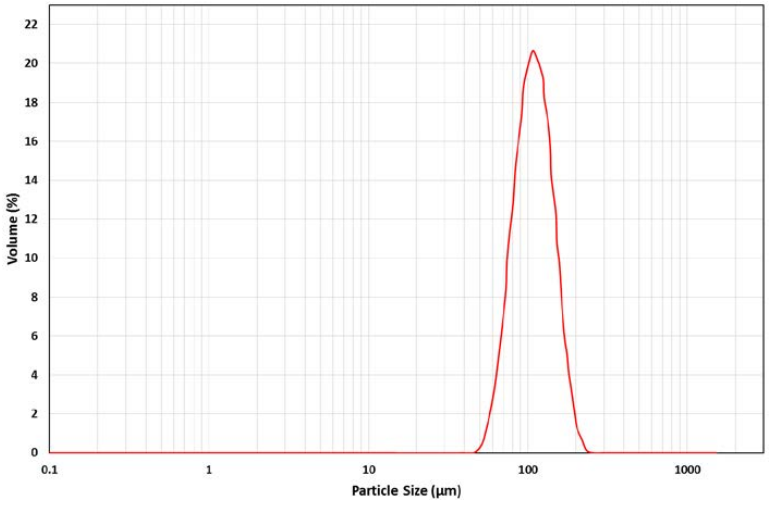

Figure 1. Particle size distribution of the feedstock powder.

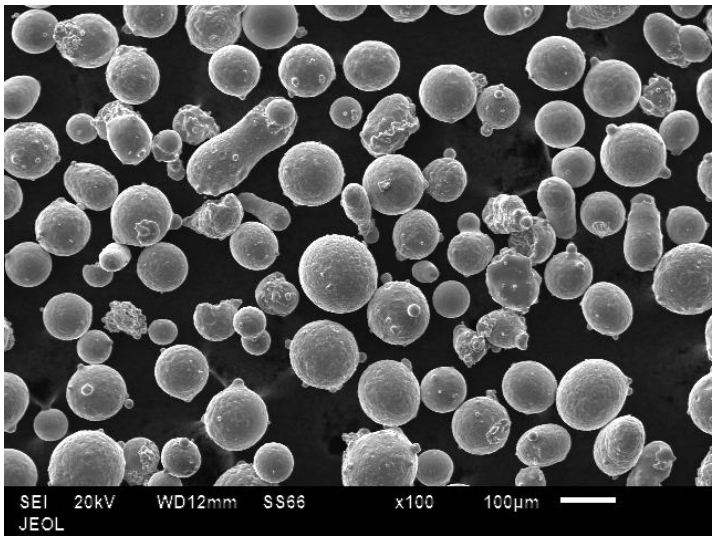

Figure 2. Morphology of γ-TiAl powder particles observed by scanning electron microscope.

Figure 3 shows CAD designs of our porous structure blocks. The blocks had 17 mm sides and a 19 mm height, and the struts had a square cross-section. By fixing the external dimensions of the blocks, the strut thickness was the only design parameter that varied to obtain different pore volume proportions. The theoretical pore volume proportions worked out to be 77%, 68%, and 54% for blocks with struts of 0.5, 1, and 1.5 mm thickness, respectively. These particular pore volumes were chosen because of the fact that at least 50% porosity is necessary in an implant for satisfactory bone ingrowth [18], and at the same time each pore should be in the range 500–2000 μm [6]. In the current study, the pore size of the entire samples was conceived to be 2500 μm in all three dimensions.

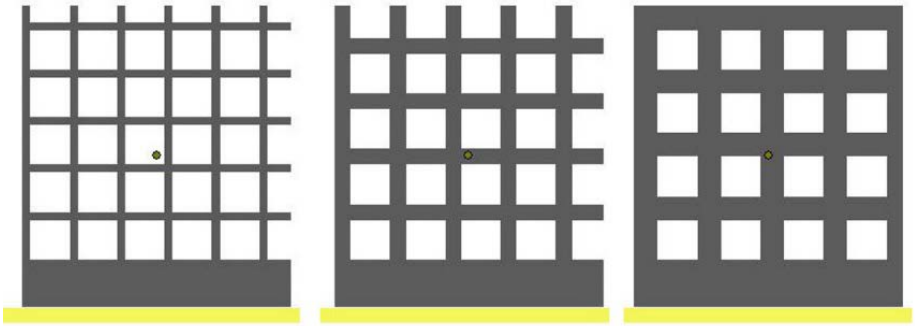

Figure 3. Porous designs with various strut thickness: 0.5 mm (**left**), 1 mm (**middle**), and 1.5 mm (**right**).

Fabricating porous structures using EBM is challenging because of such structure's fine features and discrete melt cross-sectional areas, making the scan strategy—how the beam scans when melting a given region—especially important. Typically, in EBM, the beam draws the border (contouring) and then scans the interiors (hatching). However, this "contour-and-hatch" strategy is meant for producing large feature sizes when seen against the small beam diameter (0.2–0.5 mm). Thus, in the modified scan strategy, we completely avoided the contour scan, using only the hatch scan. Table 1 shows the processing parameters that we varied during the experiments.

Table 1. EBM settings for fabricating various porous designs.

Strut Size (mm)	Beam Current (mA)	Scan Strategy
0.5 1 1.5	6, 12, and 18	Standard (contouring + hatching);
0.5 1 1.5	18	Modified (only hatching)

We produced porous γ-TiAl samples using various combinations of processing parameters, and then evaluated these samples' integrity. Discontinuities in strut formation were analyzed using scanning electron microscopy (SEM; JSM-6610LV, JEOL, Tokyo, Japan). After cutting the samples in the middle along vertical (*Z*) and horizontal (*XY*) directions with respect to the build direction, we observed them using optical microscopy (Axio Scope A1, Carl Zeiss, Oberkochen, Germany). This method will reveal asymmetry, if any, between the horizontal and vertical struts. To understand how the beam current and scan strategy affect the grain structure and phase evolution of the samples, we also examined their microstructures with optical microscopy. For this purpose, samples were etched with modified Kroll's agent (10 vol. % HF, 12 vol. % HNO_3, 85 vol. % H_2O).

Microcomputed tomography (μ-CT, General Electric, Wunstorf, Germany) was used to detect and analyze any defects and imperfections formed within the struts. This technique can measure the total open and closed porosity within a sample, and it provides a glimpse of the interior structure (non-destructive evaluation) without physical cutting or polishing. μ-CT studies were performed using a Phoenix VTomeX L240 micro-CT system (General Electric, Wunstorf, Germany) with X-ray settings of 120 kV and 160 μA. Beam filters were used to reduce beam hardening artefacts, and the scan resolution was 20 μm. The compressive strength of the cubes was analyzed using a Zwick Z100 Tester (Zwick Roell AG, Ulm, Germany) attached with a 100kN load cell and at a crosshead travel speed of 1 mm/min.

3. Results and Discussion

Initially, we used the standard scan strategy to produce blocks with struts of various sizes by just varying the current (Figure 4). This strategy produced 1 and 1.5 mm struts, but failed to produce 0.5 mm struts at any beam current. The failed builds had sections of only the horizontal struts; vertical struts that are supposed to connect the horizontal sections were completely absent. The beam diameter in EBM is 0.1–0.4 mm [19–21], which is on a par with 0.5 mm strut dimension. A standard scan strategy in EBM has two stages: contouring followed by hatching. During the contour run, the beam traces the periphery of the cross-section to be melted. Generally, the contour scanning beam has lower intensity. The main purpose of the contour run is to isolate the surrounding powder from the highly intense hatching scan to come. Contour scanning produces a smoother surface because it limits sintering of adjacent powder to the build walls. However, for especially fine cross-sections, such as those of 0.5 mm struts, the contour run would leave no space for hatching, leading to insufficient melting and a failed build.

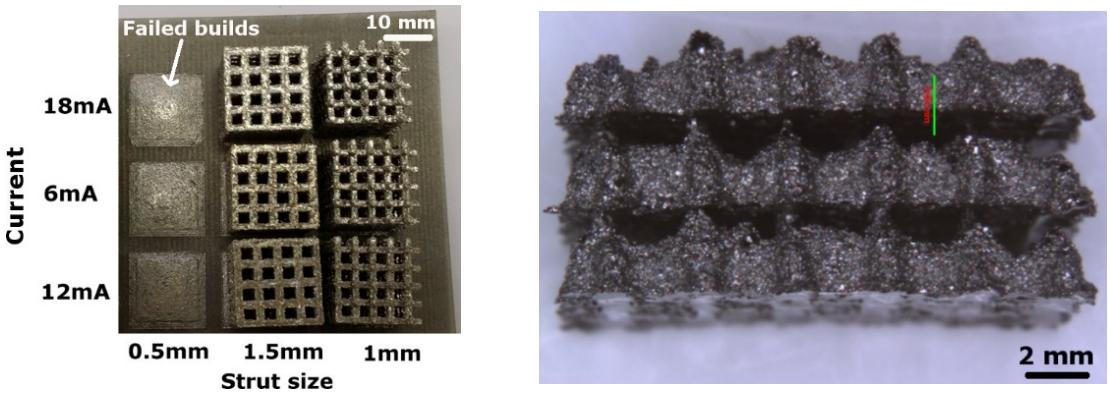

Figure 4. γ-TiAl porous structures built by EBM using the standard scan strategy (**left**); vertically disconnected layers in a failed build of the 0.5 mm strut (**right**).

Figure 5 shows a cross-section of a 1.5 mm strut produced using the standard scan strategy. Figure 6 shows a magnified image of one vertical strut. The vertical strut is ~1.37 mm wide, slightly narrower than the designed size of 1.5 mm. In contrast, the horizontal struts are much thicker (~2.05 mm) than the design. Heinl *et al.* also observed thicker horizontal struts and thinner vertical struts in Ti-6Al-4V porous structures [22]. The beam placement mainly controls the size accuracy of the vertical strut, while the resolution of the stacked layers and the table movement control the size accuracy of the horizontal struts. This process overbuilds or underbuilds the horizontal struts if the designed strut size is not an integer multiple of the layer thickness.

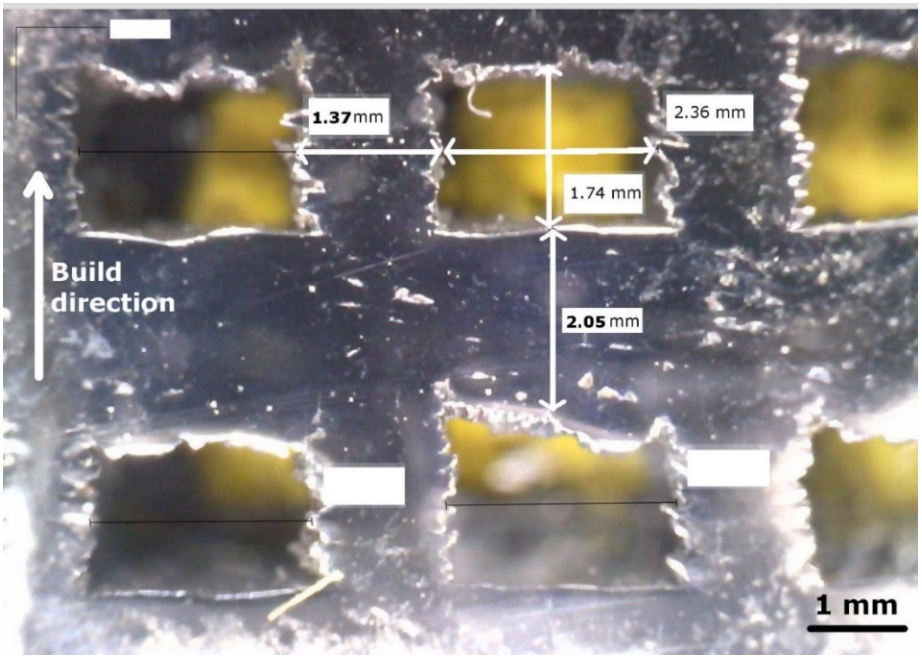

Figure 5. Macro image of 1.5 mm vertical struts produced using the standard scan strategy (cross-section along the Z-direction).

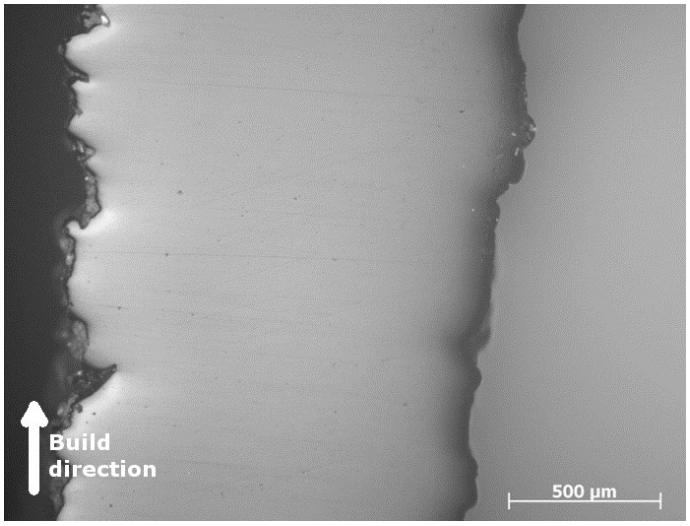

Figure 6. High-magnification optical micrograph showing 1.5 mm vertical strut produced with a standard scan strategy.

Even within a single horizontal strut, differences appeared between the top and bottom surfaces. For example, Figure 5 shows a top surface that is flatter and smoother than the bottom. During a build, the input heat mainly conducts downwards, causing the bottom surface to attract underlying loose powder and sinter it. Since there is no molten layer on the top surface, the colder powder sitting on it does not sinter as much as the bottom surface.

In the *XY* plane, the horizontal struts were uniform in size (Figure 7), and the pores were closer to square in shape (~2.56 × 2.55 mm). In the *Z* plane, though, the pores were more rectangular (~2.36 × 1.74 mm) (Figure 5). This difference means that the pores tend to be anisotropic in EBM structures. If this anisotropy is undesirable, the horizontal and vertical struts should then be designed with different sizes.

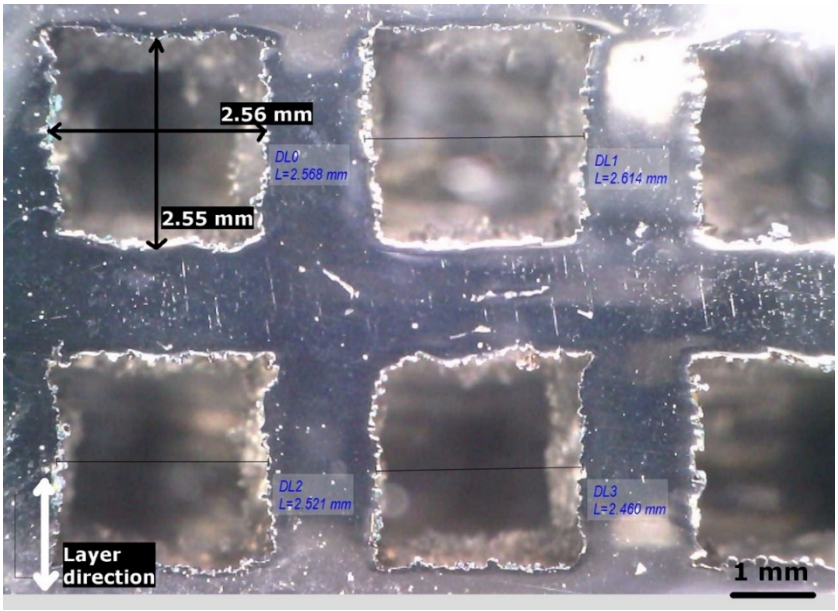

Figure 7. Macro image of 1.5 mm horizontal struts produced using standard scan strategy (cross-section along *XY* direction).

The vertical struts had jagged surfaces (Figure 8). Discrete layers added one over the other lead to the jagged vertical surfaces. This was not the only reason though; complex melt pool dynamics—how much the melt pools wets the underlying solidified layer and how much the melt pool entraps the adjacent powder particles—also determine the surface quality [23]. In general, the surface quality can be improved by reducing individual layer thickness. However, the basic size of the powder particles limits how thin a layer could be spread. Furthermore, very thin layers increase the total build time.

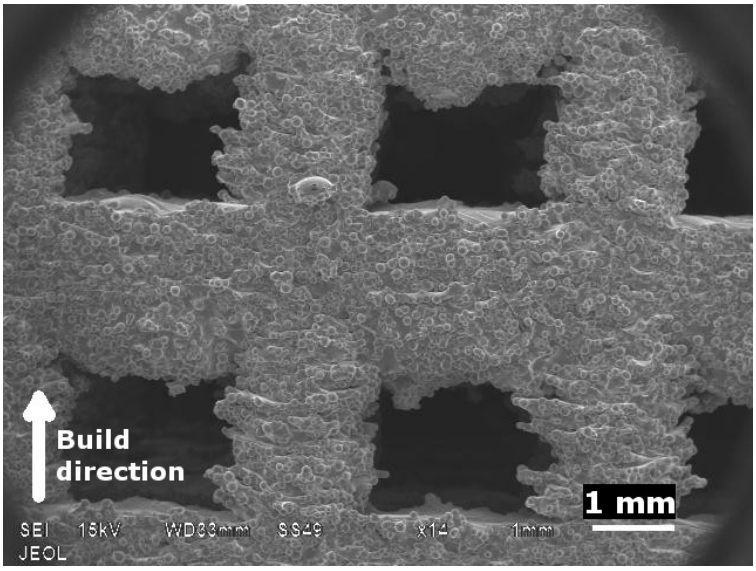

Figure 8. SEM image showing jagged vertical struts produced using standard scan strategy (1.5 mm strut).

3.1. Modified Scan Strategy

To avoid the problem of insufficient space for the hatching scan, the contour scan was removed in the next attempt. EBM experiments were later performed with this modified scan strategy. To ensure sufficient heat input, we selected a maximum beam current of 18 mA. This process successfully produced 0.5 mm struts along with the other strut sizes (Figure 9).

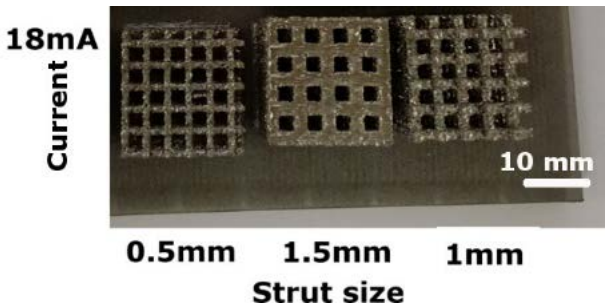

Figure 9. Intact γ-TiAl porous blocks built with 0.5 mm struts by EBM with the modified scan strategy.

Even at such a small length of 0.5 mm, both the horizontal and vertical struts were continuous and displayed no evidence of major defects (Figure 10). The modified scan strategy also improved the quality of the horizontal struts in samples with larger struts (Figure 11). In these samples, only a little powder appeared sintered to the bottom surfaces. The pores were relatively square. These advantages bolster the case for discarding the contour scan altogether while building fine porous structures using EBM.

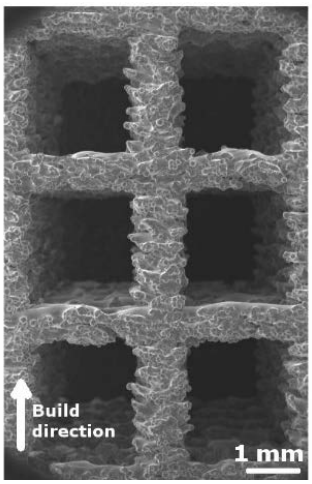

Figure 10. Intact 0.5 mm struts produced using the modified contour strategy.

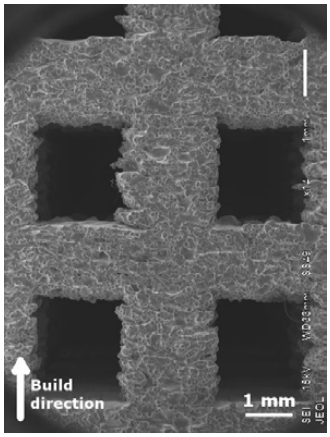

Figure 11. Better-quality surfaces of horizontal struts produced with the modified scan strategy (1.5 mm strut).

Figure 12 shows a vertical strut produced with the modified scan strategy. Here, the average strut size was ~1.8 mm, which is indeed thicker than the intended size of 1.5 mm. Note that a standard scan strategy produced a thinner strut (Figure 6). Since the modified scan strategy has no contour scan, the intense hatching beam scanned the whole cross-section. This process generated a larger melt volume, producing thicker struts.

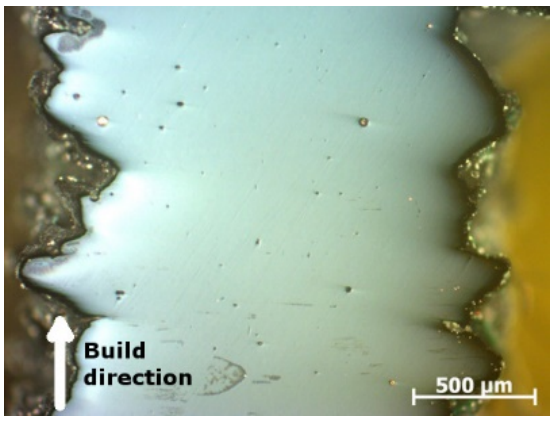

Figure 12. Vertical 1.5 mm strut built with the modified scan strategy.

3.2. Effect of Beam Current

Figure 13 shows how the beam current affected the microstructures of the struts. These microstructures came from the middle region of the samples in the build (vertical) direction. Further, the microstructures were almost the same even in the top and bottom regions (not shown here). This was apparently due to the limited height (19 mm) of the samples in our study.

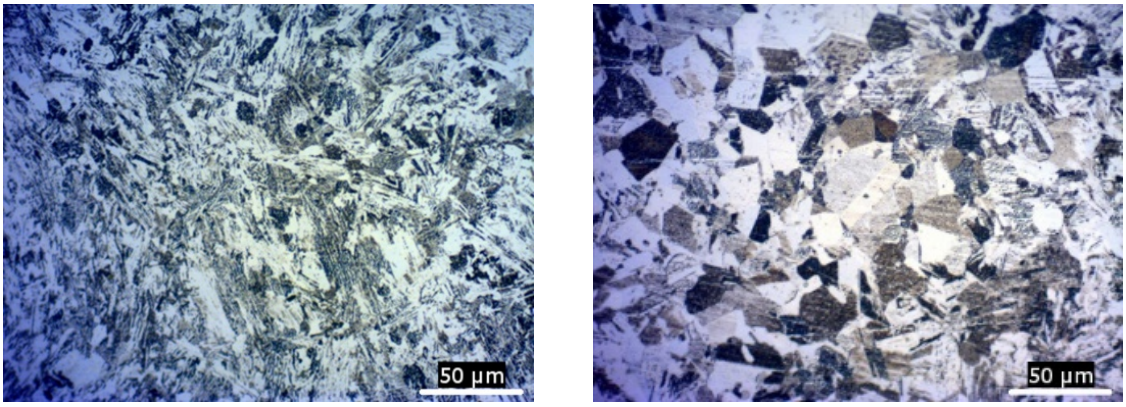

Figure 13. A lamellar microstructure produced at a higher beam current of 18 mA (**left**), compared to an equiaxed structure produced at 6 mA (**right**); both with the standard scan strategy.

Typically, the microstructure for the composition chosen in the current work should consist of two phases: γ(TiAl) and $\alpha 2$(Ti_3Al). Depending upon the dispersion of each of these phases, the microstructure can vary from near gamma to fully lamellar, with a duplex type in between. In the near gamma type, the grains are mainly γ-phase, whereas $\alpha 2$-phase can be found only along the grain boundaries. At the other extreme, these two phases can co-exist side-by-side as lamellae. A mix of these two types of microstructures results in the duplex type, wherein lamellar colonies would be seen amidst the equiaxed γ grains. The microstructure that eventually settles down in the dual phase TiAl compositions ultimately depends on the processing conditions, mainly the temperature. For instance, elemental powders having composition (48% Al-2% Cr-2% Nb) similar to the present work, when consolidated by the powder metallurgy route at a temperature of 1400 °C resulted in a fully lamellar microstructure, while at a lesser temperature of 1200 °C, the same powder resulted in a duplex structure [24]. Likewise, in the current study, a higher beam current produced a microstructure dominated by coarse lamellar structure with few equiaxed grains (Figure 13), but when the current was lowered, more equiaxed regions started to emerge (Figure 13 right). Higher beam currents mean more heating of the current and the underlying layers. The best microstructure from a ductility point of view, however, is the duplex type [25] , and this was seen in the case of a modified scan strategy (Figure 14). It is interesting to note that Biamino *et al.* [25] achieved the duplex microstructure in EBM produced γ-TiAl after heat treating the near equiaxed microstructure. The fact that we observed duplex microstructure in as-produced EBM samples suggests that the electron beam subjected the underlying regions to the same kind of heat treatment. Hence, it cannot be overemphasized how important was the beam current and scan strategy in obtaining an optimum microstructure. In other words, both these parameters influenced the processing temperature.

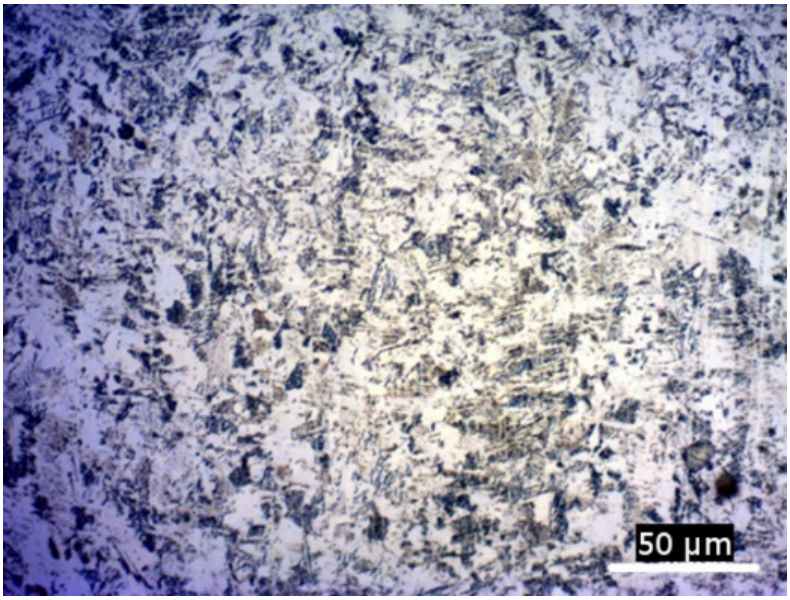

Figure 14. Duplex microstructure produced with the modified scan strategy.

Table 2 shows the µ-CT analysis of the porous γ-TiAl blocks. The 0.5 mm struts had a surface-to-volume ratio almost twice that of the 1 mm struts. Such a high ratio is desirable for material-to-bone adhesion in bio-implants [26].

Table 2. Surface-to-volume ratio estimated by µ-CT.

Strut Thickness (mm)	Scan Strategy	Surface Area/Volume Ratio (mm^{-1})
1	Standard	1.19
1	Modified	4.63
0.5	Modified	8.88

Figure 15 gives a µ-CT image of the 0.5 mm struts. The 2D slice (top left image in Figure 15) shows scattered discontinuities along the span of the struts. This may create an impression that the struts were broken at these positions, which is not true, however. If we take into account that it is a 2D slice, it is quite possible that an adjacent slice could envelop a discontinuity, thus making it a closed pore rather than a total rupture in the strut. Hence, a 3D illustration (bottom right in Figure 15) would prove more valuable in such cases. Indeed, quantitative analysis revealed internal porosity to be minimal (~0.19%) (Table 3). The diameter of the largest internal pore was ~0.43 mm, meaning at least a portion of the material was constantly present along the strut. Since the currently used scan resolution is 20 µm, pores smaller than this dimension could not be detected by the µ-CT test. For detecting such small pores, one has to resort to alternate techniques such as 2-D image analysis.

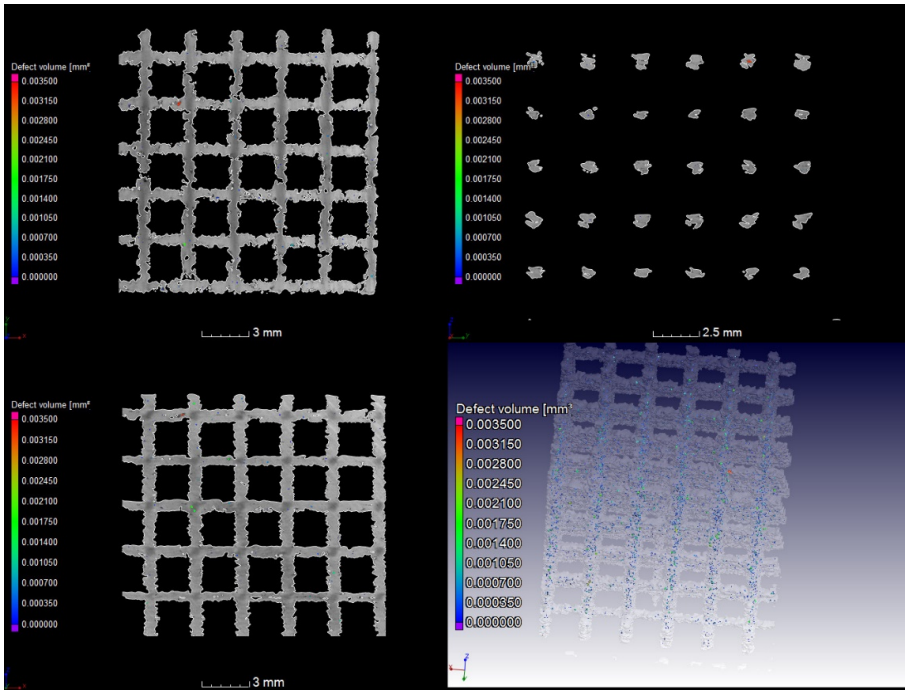

Figure 15. Internal defect volume analyzed by μ-CT (0.5 mm strut).

Table 3. Quantitative assessment of internal porosity by μ-CT.

Strut Thickness (mm)	Scan Strategy	Largest Internal Pore Diameter (mm)	Average Internal Porosity (vol. %)
1	Standard	1.19	0.25
1	Modified	0.52	0.21
0.5	Modified	0.43	0.19

The modified scan strategy proved to be better even for producing thicker struts (Table 3). This strategy reduced both the size and total volume of internal pores. Figure 16 shows the extent of divergence observed in the built specimens from the STL dimensions. The divergence was lower for the samples produced with the modified scan strategy. As discussed earlier, this occurred because the modified scan strategy reduced powder sintering to the bottom of the horizontal struts. This aspect ultimately narrowed down the divergence from the actual values.

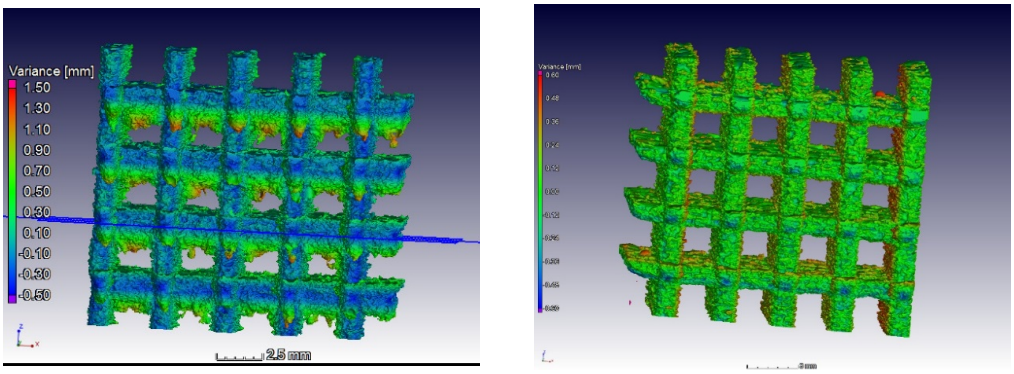

Figure 16. Degree of variance from original STL file (1 mm strut): standard (**left**) and modified (**right**) scan strategies.

3.3. Compression Test

Generally, a compression curve depends on the material and pore structure. For example, Hernández-Nava *et al.* showed that identical structures of Ti-6Al-4V and aluminum had different compression behavior [27]. Table 4 lists the results of the compression test performed on the porous blocks. Figure 17 demonstrates how the strut size affected compressive mechanical behavior of the γ-TiAl samples. The diversity in the shapes of compression curves was caused by the varying pore volume proportion. The strut thickness seems to be the dominant influence in mechanical properties, such as modulus and peak stress. Structures with 1.5 mm struts had better mechanical properties. For a given strut size, the beam current had no significant effect.

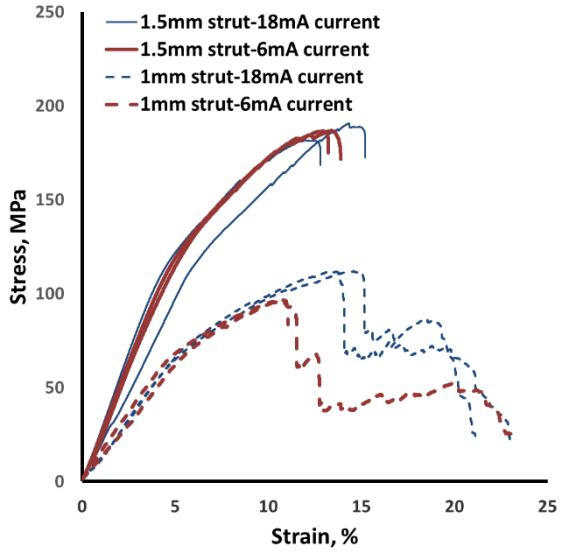

Figure 17. Effect of strut size on compressive properties in γ-TiAl porous structures produced using a standard scan strategy (Note: This scan strategy failed to build 0.5 mm strut samples as indicated in Table 4).

Table 4. Compression test results for different porous designs.

Sample Number	Sample Conditions			Young's Modulus (GPa)	Peak Compressive Stress σ (MPa)
	Strut Size (mm)	Current (mA)	Scan Strategy		
1	1.5	18	Standard	2.39 ± 0.51	186 ± 6.22
2	1.5	12	Standard	Not tested	Not tested
3	1.5	6	Standard	2.59 ± 0.02	186 ± 0.20
4	1	18	Standard	1.46 ± 0.04	111 ± 0.07
5	1	12	Standard	1.71 ± 0.02	111 ± 1.07
6	1	6	Standard	1.35 ± 0.07	96 ± 0.71
7	0.5	18	Standard	Build failed	Build failed
8	0.5	12	Standard	Build failed	Build failed
9	0.5	6	Standard	Build failed	Build failed
10	1.5	18	Modified	2.67 ± 0.16	255 ± 5.59
13	1	18	Modified	1.91 ± 0.07	125 ± 7.76
16	0.5	18	Modified	0.81 ± 0.05	26 ± 0.33

In general, the compressive stress-strain curve of a porous sample has three regions. The first is the linear elastic deformation region, in which the cells are bent or compressed elastically. The second stage is the plateau region, in which the cell edges yield by bending. In the third stage, the cell experiences strain hardening; it is in this stage that the stress maximizes [28].

The compressive stress-strain graphs initially curve up (Figures 17–19). After the upward curving ends, the linear elastic region sets in. The upward curve is generally associated with porous structures because it takes a certain time for the machine platens to come into full contact with the specimen faces [27]. None of the curves had a distinct plateau region. The elastic region was followed by a linear plastic region. Beyond this point, the structures did not deform as a whole. Instead, they experienced local fractures, reflected in the serrations at the end of curves. This behavior of the γ-TiAl porous structures was similar to that of a porous Ti-6Al-4V structure [27,29], as both the materials are brittle and barely tolerate defects.

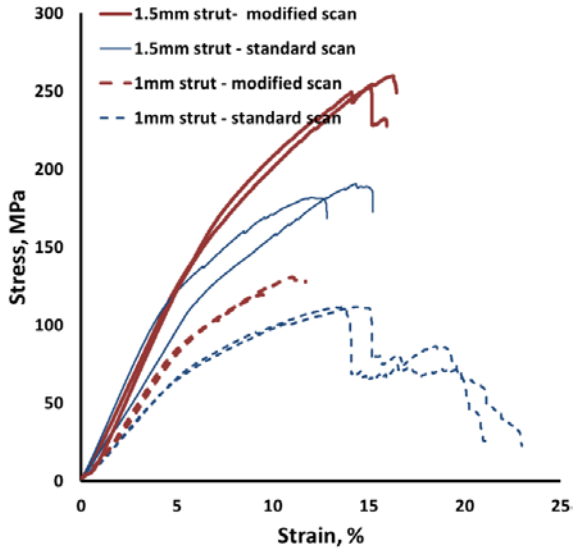

Figure 18. Effect of scan strategy on compressive properties in γ-TiAl porous structures (beam current of 18 mA).

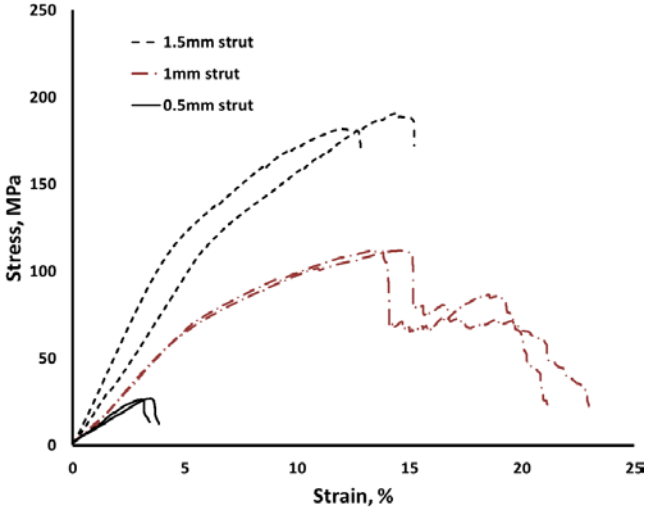

Figure 19. Effect of strut size on compressive properties of γ-TiAl porous structures (beam current of 18 mA).

Figure 18 explains the role of the scan strategy. For a given strut size and beam current, the sample produced with the modified scan strategy showed a larger peak stress than that produced with the standard strategy. As was discussed above (Section 3.2), modified scan strategy resulted in a duplex microstructure, whereas the standard scan strategy produced a lamellar microstructure. A

duplex microstructure is better as far as stress and ductility are concerned [24]. Thus, the appropriate microstructure could be said to have contributed to better compression properties. Add to this the better quality struts, and we can safely attribute the higher compression properties to the modified scan strategy.

The compression results agree well with the Ashby-Gibson theoretical model. Increasing the porosity volume decreased the Young's modulus as well as the peak stress (Table 4 and Figure 20). One of the engineering fields where a relationship between the pore volume and stiffness is of interest is powder metallurgy. Of course, in powder metallurgy the pores are assumed to be round and randomly distributed. Nevertheless, predictive equations that relate pore volume and stiffness, although drawn from a diverse field such as powder metallurgy, can serve as a generic aid for the present case. Allison *et al.* compared many such equations available in the literature related to powder metallurgy [30]. All the equations estimated a fall in stiffness with increasing pore volume fraction, similar to what was observed in the current work. The equation that Allison *et al.* concluded to be most accurate evinced a prominent drop in stiffness when the pore fraction went above 20%. This, too, substantiates our observation about the larger drop in modulus for the highly porous 0.5 mm strut samples (Figure 20). The possibility of producing defined porous components by an additive manufacturing route, quite unlike powder metallurgy, encouraged Choren *et al.* [31] to seek similar relationships, if any available. Again, most of the scrutinized equations predicted a non-linear drop in modulus in regimes up to 40% porosity. Beyond this range, however, Choren *et al.* lamented about a lack of satisfactory models.

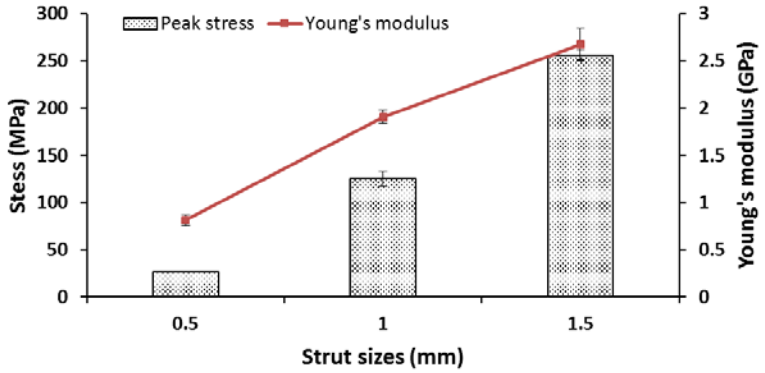

Figure 20. Compressive peak stress based on the total cross-sectional area of the samples (modified scan strategy) (see also Table 4).

The compression values achieved in our study have practical importance in fabricating bio-implants, whose stiffness must be matched to the stiffness of patients' bones to minimize stress shielding. We obtained stiffness of ~0.81 GPa with 0.5 mm struts which is close to that of the trabecular bone (~1.08 GPa) [22]. Jayanthi *et al.* produced Ti-6Al-4V porous structures with a stiffness of 0.57 GPa [6], but their peak stress was a mere 7 MPa. With the same Ti-6Al-4V alloy, Hernandez *et al.* achieved a stiffness of 0.65 GPa and a peak stress of 11.7 MPa [27]. We produced 0.5 mm struts with almost the same stiffness but with a higher peak stress of 26 MPa, allowing these γ-TiAl implants to withstand greater loads while protecting adjoining natural bone from the stress-shielding effect.

Compressive properties were also evaluated taking into account only the strut area that contributes to the load bearing ability of the porous samples (Figure 21). The trend in the peak stress variation was similar to when the total sample cross-section was considered, *i.e.*, the stress decreased with strut size. The drop in the stress from 1 mm to 0.5 struts was more drastic than from 1.5 mm to 1 mm struts. As the struts became thinner and thinner, the surface area increased (Table 2); consequently, the possibility of occurrence of surface defects also increases which ultimately affected the peak stress. The trend in Young's modulus, however, was converse to the peak stress: the Young's modulus was higher in thinner struts. This means that a unit area of material distributed into a greater number of

load bearing columns behaved in a stiffer manner than when the same unit area of the material end up in a thicker, but with fewer number of columns. As previously mentioned, the linear elastic region of porous designs is shaped by how the cells bend elastically. The framework in 0.5 mm strut samples was fashioned from more number of struts and pores than other samples. Greater number of such cells, then, must have supported each other from easily bending and, hence, becoming stiffer in the process.

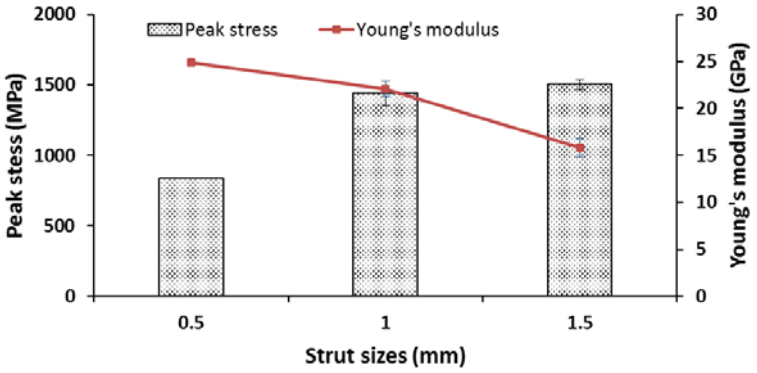

Figure 21. Compressive properties after correcting for the designed cross-sectional area of the struts (modified scan strategy).

4. Conclusions

In this study, we used electron beam melting to produce porous structures from γ-TiAl. Samples with overall pore volumes of 54%, 68%, and 77% were produced. Keeping the pore dimensions constant, we only changed the strut size to determine the final pore volume proportion. Three beam currents and two scan strategies were analyzed for their effect on the strut quality. The main conclusions are as follows:

1. The standard scan strategy (contour and hatch) produced all the struts except the 0.5 mm-thick ones, which failed because the scan strategy could not build the thin vertical struts. Even higher beam current could not create the 0.5 mm struts using this scan strategy.
2. With a standard scan strategy, powder sintered to the underside of the horizontal struts, making them bulkier than designed. The differences in thickness between the vertical and horizontal struts caused anisotropic pore shapes.
3. A modified scan strategy (only hatching) produced 0.5 mm struts. This was possible because, in the modified scan strategy, the intense hatching beam imparted greater energy to the narrow regions required to build thin vertical struts.
4. The modified scan strategy gave better results than the standard strategy, even for thicker struts. The modified strategy reduced the amount of powder sintered to the bottoms of the horizontal struts which, in turn, produced pores closer to the design in all directions.
5. The stiffness of the 0.5 mm strut structures was ~0.8 GPa, which is closer to the stiffness of a trabecular bone. Additionally, these fine structures had a decent peak stress of 26 MPa. Thus, by tuning the thicknesses of the struts and modifying the scan strategy, we could produce porous structures of γ-TiAl with the desired mechanical properties by using EBM. This attribute will play a critical role in manufacturing bio-implants specific to each patient.

In the current study, probably because the samples were small, we could remove any loose powder, even from the interiors, by high-pressure powder blasting. However, this method may not work well enough for larger samples; thus, other powder-removal techniques should be considered in any future works.

Acknowledgments: This project was funded by the National Plan for Science, Technology and Innovation (MAARIFAH), King Abdul-Aziz City for Science and Technology, Kingdom of Saudi Arabia, Award Number (11-ADV1494-02).

Author Contributions: Ashfaq Mohammad conceived and designed the study. Khaja Moiduddin, Muneer Khan Mohammed, and Abdulrahman Alomar joined Ashfaq Mohammad in conducting the EBM experiments. Ravi Kottan Renganayagalu and Ashfaq Mohammad characterized and analyzed the microstructure and mechanical properties. Abdulrahman M. Alahmari and Ashfaq Mohammad drafted the manuscript and critically reviewed it.

Conflicts of Interest: The authors declare no conflict of interest.

References

1. Roy, S.; Panda, D.; Khutia, N.; Chowdhury, A.R.; Roy, S.; Panda, D.; Khutia, N.; Chowdhury, A.R. Pore geometry optimization of titanium (Ti6Al4V) alloy, for its application in the fabrication of customized hip implants. *Int. J. Biomater.* **2014**. [CrossRef]
2. Ikeo, N.; Ishimoto, T.; Fukuda, H.; Nakano, T. Fabrication and characterization of porous implant products with aligned pores by EBM method for biomedical application. *Adv. Mater. Res.* **2011**, *409*, 142–145. [CrossRef]
3. Xiong, J.; Mines, R.; Ghosh, R.; Vaziri, A.; Ma, L.; Ohrndorf, A.; Christ, H.J.; Wu, L. Advanced micro-lattice materials. *Adv. Eng. Mater.* **2015**, *17*, 1253–1264. [CrossRef]
4. Lv, J.; Jia, Z.; Li, J.; Wang, Y.; Yang, J.; Xiu, P.; Zhang, K.; Cai, H.; Liu, Z. Electron beam melting fabrication of porous Ti6Al4V scaffolds: Cytocompatibility and osteogenesis. *Adv. Eng. Mater.* **2015**, *17*, 1391–1398. [CrossRef]
5. Murr, L.; Gaytan, S.; Martinez, E. Fabricating functional Ti-alloy biomedical implants by additive manufacturing using electron beam melting. *J. Biotechnol. Biomater.* **2012**. [CrossRef]
6. Parthasarathy, J.; Starly, B.; Raman, S.; Christensen, A. Mechanical evaluation of porous titanium (Ti6Al4V) structures with electron beam melting (EBM). *J. Mech. Behav. Biomed. Mater.* **2010**, *3*, 249–259. [CrossRef] [PubMed]
7. Li, S.; Zhao, S.; Hou, W.; Teng, C.; Hao, Y.; Li, Y.; Yang, R.; Misra, R.D.K. Functionally graded Ti-6Al-4V meshes with high strength and energy absorption. *Adv. Eng. Mater.* **2016**, *18*, 34–38. [CrossRef]
8. Martinez, E.; Murr, L.E.; Hernandez, J.; Pan, X.; Amato, K.; Frigola, P.; Terrazas, C.; Gaytan, S.; Rodriguez, E.; Medina, F.; *et al*. Microstructures of niobium components fabricated by electron beam melting. *Metallogr. Microstruct. Anal.* **2013**, *2*, 183–189. [CrossRef]
9. Cormier, D.; Harrysson, O.; West, H. Characterization of H13 steel produced via electron beam melting. *Rapid Prototyp. J.* **2004**, *10*, 35–41. [CrossRef]
10. Ramirez, D.A.; Murr, L.E.; Li, S.J.; Tian, Y.X.; Martinez, E.; Martinez, J.L.; Machado, B.I.; Gaytan, S.M.; Medina, F.; Wicker, R.B. Open-cellular copper structures fabricated by additive manufacturing using electron beam melting. *Mater. Sci. Eng. A* **2011**, *528*, 5379–5386. [CrossRef]
11. Cormier, D.; Harrysson, O.; Mahale, T.; West, H. Freeform fabrication of titanium aluminide via electron beam melting using prealloyed and blended powders. *Adv. Mater. Sci. Eng.* **2008**. [CrossRef]
12. Aspinwall, D.K.; Dewes, R.C.; Mantle, A.L. The Machining of γ-TiAl intermetallic alloys. *CIRP Ann. Manuf. Technol.* **2005**, *54*, 99–104. [CrossRef]
13. Tetsui, T.; Shindo, K.; Kaji, S.; Kobayashi, S.; Takeyama, M. Fabrication of TiAl components by means of hot forging and machining. *Intermetallics* **2005**, *13*, 971–978. [CrossRef]
14. Rivera-Denizard, O.; Diffoot-Carlo, N.; Navas, V.; Sundaram, P.A. Biocompatibility studies of human fetal osteoblast cells cultured on gamma titanium aluminide. *J. Mater. Sci. Mater. Med.* **2008**, *19*, 153–158. [CrossRef] [PubMed]
15. Santiago-Medina, P.; Sundaram, P.A.; Diffoot-Carlo, N. The effects of micro arc oxidation of gamma titanium aluminide surfaces on osteoblast adhesion and differentiation. *J. Mater. Sci. Mater. Med.* **2014**, *25*, 1577–1587. [CrossRef] [PubMed]
16. Hernandez, J.; Murr, L.E.; Gaytan, S.M.; Martinez, E.; Medina, F.; Wicker, R.B. Microstructures for two-phase gamma titanium aluminide fabricated by electron beam melting. *Metallogr. Microstruct. Anal.* **2012**, *1*, 14–27. [CrossRef]

17. Murr, L.E.; Esquivel, E.V.; Quinones, S.A.; Gaytan, S.M.; Lopez, M.I.; Martinez, E.Y.; Medina, F.; Hernandez, D.H.; Martinez, E.; Martinez, J.L.; *et al*. Microstructures and mechanical properties of electron beam-rapid manufactured Ti-6Al-4V biomedical prototypes compared to wrought Ti-6Al-4V. *Mater. Charact.* **2009**, *60*, 96–105. [CrossRef]
18. Arabnejad, S.; Johnston, R.B.; Pura, J.A.; Singh, B.; Tanzer, M.; Pasini, D. High-strength porous biomaterials for bone replacement: A strategy to assess the interplay between cell morphology, mechanical properties, bone ingrowth and manufacturing constraints. *Acta Biomater.* **2016**, *30*, 345–356. [CrossRef] [PubMed]
19. Attar, E. *Simulation of Selective Electron Beam Melting Processes*; VDM Publishing: Saarbrücken, Germany, 2011.
20. Shen, N.; Chou, K. Thermal modeling of electron beam additive manufacturing process: Powder sintering effects. In Proceedings of the ASME 2012 International Manufacturing Science and Engineering Conference, Notre Dame, IN, USA, 4–8 June 2012; pp. 287–295.
21. Arce, A.N. *Thermal Modeling and Simulation of Electron Beam Melting For Rapid Prototyping on Ti6Al4V Alloys*; North Carolina State University: Raleigh, NC, USA, 2013.
22. Heinl, P.; Müller, L.; Körner, C.; Singer, R.F.; Müller, F.A. Cellular Ti-6Al-4V structures with interconnected macro porosity for bone implants fabricated by selective electron beam melting. *Acta Biomater.* **2008**, *4*, 1536–1544. [CrossRef] [PubMed]
23. Körner, C.; Attar, E.; Heinl, P. Mesoscopic simulation of selective beam melting processes. *J. Mater. Process. Technol.* **2011**, *211*, 978–987. [CrossRef]
24. Kothari, K.; Radhakrishnan, R.; Sudarshan, T.S.; Wereley, N.M. Characterization of rapidly consolidated γ-TiAl. *Adv. Mater. Res.* **2012**, *1*, 51–74. [CrossRef]
25. Biamino, S.; Penna, A.; Ackelid, U.; Sabbadini, S.; Tassa, O.; Fino, P.; Pavese, M.; Gennaro, P.; Badini, C. Electron beam melting of Ti-48Al-2Cr-2Nb alloy: Microstructure and mechanical properties investigation. *Intermetallics* **2011**, *19*, 776–781. [CrossRef]
26. Feller, L.; Jadwat, Y.; Khammissa, R.A.G.; Meyerov, R.; Schechter, I.; Lemmer, J.; Feller, L.; Jadwat, Y.; Khammissa, R.A.G.; Meyerov, R.; *et al*. Cellular responses evoked by different surface characteristics of intraosseous titanium implants. *BioMed Res. Int.* **2015**. [CrossRef] [PubMed]
27. Hernández-Nava, E.; Smith, C.J.; Derguti, F.; Tammas-Williams, S.; Léonard, F.; Withers, P.J.; Todd, I.; Goodall, R. The effect of density and feature size on mechanical properties of isostructural metallic foams produced by additive manufacturing. *Acta Mater.* **2015**, *85*, 387–395. [CrossRef]
28. Li, X.; Wang, C.; Zhang, W.; Li, Y. Fabrication and characterization of porous Ti6Al4V parts for biomedical applications using electron beam melting process. *Mater. Lett.* **2009**, *63*, 403–405. [CrossRef]
29. Wauthle, R.; Ahmadi, S.M.; Yavari, S.A.; Mulier, M.; Zadpoor, A.A.; Weinans, H.; van Humbeeck, J.; Kruth, J.P.; Schrooten, J. Revival of pure titanium for dynamically loaded porous implants using additive manufacturing. *Mater. Sci. Eng. C Mater. Biol. Appl.* **2015**, *54*, 94–100. [CrossRef] [PubMed]
30. Allison, P.G.; Horstemeyer, M.F.; Brown, H.R. Modulus dependence on large scale porosity of powder metallurgy steel. *J. Mater. Eng. Perform.* **2012**, *21*, 1422–1425. [CrossRef]
31. Choren, J.A.; Heinrich, S.M.; Silver-Thorn, M.B. Young's modulus and volume porosity relationships for additive manufacturing applications. *J. Mater. Sci.* **2013**, *48*, 5103–5112. [CrossRef]